

# Observation of ultracold atomic bubbles in orbital microgravity

<https://doi.org/10.1038/s41586-022-04639-8>

Received: 12 August 2021

Accepted: 14 March 2022

Published online: 18 May 2022

 Check for updates

R. A. Carollo<sup>1,6</sup>, D. C. Aveline<sup>2,6</sup>, B. Rhyno<sup>3</sup>, S. Vishveshwara<sup>3</sup>, C. Lannert<sup>4,5</sup>, J. D. Murphree<sup>1</sup>, E. R. Elliott<sup>2</sup>, J. R. Williams<sup>2</sup>, R. J. Thompson<sup>2</sup> & N. Lundblad<sup>1</sup>✉

Substantial leaps in the understanding of quantum systems have been driven by exploring geometry, topology, dimensionality and interactions in ultracold atomic ensembles<sup>1–6</sup>. A system where atoms evolve while confined on an ellipsoidal surface represents a heretofore unexplored geometry and topology. Realizing an ultracold bubble—potentially Bose–Einstein condensed—relates to areas of interest including quantized-vortex flow constrained to a closed surface topology, collective modes and self-interference via bubble expansion<sup>7–17</sup>. Large ultracold bubbles, created by inflating smaller condensates, directly tie into Hubble-analogue expansion physics<sup>18–20</sup>. Here we report observations from the NASA Cold Atom Lab<sup>21</sup> facility onboard the International Space Station of bubbles of ultracold atoms created using a radiofrequency-dressing protocol. We observe bubble configurations of varying size and initial temperature, and explore bubble thermodynamics, demonstrating substantial cooling associated with inflation. We achieve partial coverings of bubble traps greater than one millimetre in size with ultracold films of inferred few-micrometre thickness, and we observe the dynamics of shell structures projected into free-evolving harmonic confinement. The observations are among the first measurements made with ultracold atoms in space, using perpetual freefall to explore quantum systems that are prohibitively difficult to create on Earth. This work heralds future studies (in orbital microgravity) of the Bose–Einstein condensed bubble, the character of its excitations and the role of topology in its evolution.

Although the techniques for the generation of ultracold atomic bubbles have been known since 2001<sup>22</sup>, terrestrial gravity prevents the observation of these configurations, as the trapped sample simply sags to the lower fraction of the given shell trap, forming a conventional (if distorted) ultracold ensemble. With the recent construction of the NASA Cold Atom Lab (CAL) facility and its subsequent delivery to the International Space Station and commissioning as an orbital Bose–Einstein condensate (BEC) facility<sup>21,23</sup>, experimental efforts requiring a sustained microgravity environment are now possible, including realistic possibilities for ultracold bubble physics, as recently proposed<sup>24</sup>. Here we present observations of ultracold bubbles created in microgravity aboard CAL using protocols developed to explore bubble size and temperature. We give detailed measurements of subsequent inflated bubble temperature varying as a function of initial sample temperature—linking to theory realistically modelling the CAL apparatus—and observe the effects of shell-trap removal and the resulting atomic bubble propagation in the pre-existing harmonic trap.

## Physics of bubble creation

We first summarize the atomic-physics framework for generation of ultracold bubble systems. Our creation of a shell-like confining

potential  $U(\mathbf{r})$  (where  $\mathbf{r}$  is position) for ultracold atoms stems from a theoretical proposal to generate matter-wave bubbles allowing for the study of two-dimensional (2D) BECs tightly pinned to partial coverings of the potential<sup>22,25,26</sup>. This scheme relies on a locally harmonic spin-dependent trapping potential originating in an applied magnetic field  $\mathbf{B}(\mathbf{r})$ , combined with a near-resonant oscillatory magnetic field  $\mathbf{B}_{\text{rf}}$  at radiofrequency  $\omega_{\text{rf}}$ , resulting in spatially dependent dressed atomic states<sup>27,28</sup>. Atoms in these states experience effective (dressed or adiabatic) potentials, which can be tailored such that atoms enter bubble-like configurations of diverse size and thickness. As depicted in Fig. 1, atoms in spin states  $|m\rangle$  exposed to a magnetic trapping field experience trapping potentials  $U_m(\mathbf{r}) = g_F m \mu_B |\mathbf{B}(\mathbf{r})|$ , where  $g_F$  is the Landé g-factor associated with (in our case) a given atomic hyperfine manifold of total angular momentum  $F$ ,  $m$  is the associated projection quantum number, and  $\mu_B$  is the Bohr magneton. In the presence of  $\mathbf{B}_{\text{rf}}$ , the combination of a rotating-frame transformation and the application of a rotating-wave approximation results in a dressed-picture Hamiltonian  $\mathcal{H}$ , and the creation of associated dressed potentials  $U'_m(\mathbf{r})$  (Methods). Although shell potentials for ultracold atoms have been generated and explored in several groups<sup>29–31</sup>, efforts to explore bubble-centred physics have been hampered by the presence of terrestrial gravitational potential energy  $U_g = Mgz$ , where  $M$  is atomic mass

<sup>1</sup>Department of Physics and Astronomy, Bates College, Lewiston, ME, USA. <sup>2</sup>Jet Propulsion Laboratory, California Institute of Technology, Pasadena, CA, USA. <sup>3</sup>Department of Physics, University of Illinois at Urbana-Champaign, Urbana, IL, USA. <sup>4</sup>Department of Physics, Smith College, Northampton, MA, USA. <sup>5</sup>Department of Physics, University of Massachusetts, Amherst, MA, USA.

<sup>6</sup>These authors contributed equally: R. A. Carollo, D. C. Aveline. ✉e-mail: nlundbla@bates.edu

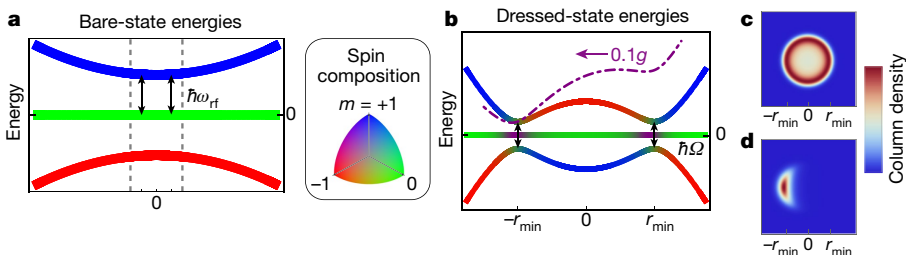


**Fig. 1 | Creating ultracold bubbles.** The illustrations are from an idealized three-level analytic model of an isotropic trap, using otherwise typical experimental parameters. **a**, Atoms are prepared in the highest-energy spin state near the minimum of a static magnetic field (blue curve). Applying a radiofrequency magnetic field of frequency  $\omega_{\text{rf}}$  and coupling strength  $\Omega$  creates spatially varying superpositions of the bare magnetic states. The dashed lines correspond to the bounds of the region in **b**. **b**, Atoms in stationary (dressed) states of the combined fields experience a dressed potential with extrema at points  $\pm r_{\text{min}}$  where the radiofrequency field is resonant. The

highest-energy dressed potential forms a double well along any axis passing through the static field's minimum; the dot-dashed purple curve shows the effect of adding a gravitational field of magnitude 0.1g. This idealized model shows how atoms congregate at the trap minimum in three dimensions, as seen in **c**. **c**, The modelled column density (optical depth: red, high; blue, low) profile of an ultracold bubble. **d**, Column density of atoms in the potential described by the purple curve in **b**, showing that a 0.1g gravitational field will prevent atoms from covering the bubble's entire surface; 1g creates even greater deformation.

and  $z$  is local vertical displacement. Preliminary schemes have been developed to cancel this gravitational tilt—using (for example) an appropriate a.c. Stark shift gradient or a radiofrequency coupling gradient—however, precise cancellation over a volume appropriate for an ultracold bubble is not yet possible<sup>32,33</sup>. Application of this technique to the CAL apparatus was recently proposed, specifically accounting for known inhomogeneities in realistic dressed potentials such as would originate from the spatial dependence of the radiofrequency field or the anharmonicity of the CAL magnetic trap<sup>24</sup>. Although an idealized bubble is spherical<sup>34</sup>, these shell potentials are generally ellipsoidal, as dictated by the aspect ratio of the generating trap.

## NASA CAL experiments and observations

We conducted these experiments in a remotely operated user facility located in low Earth orbit aboard the International Space Station (ISS). This facility, the NASA CAL, was delivered to the ISS via rocket launch in 2018 and conducted its first science runs in January 2020 before undergoing hardware upgrades. Its development and ground test process have been reported<sup>23</sup>, as has its core functionality—the generation of BECs in orbital microgravity<sup>21</sup>. The regular operation of the facility provides ultracold samples to scheduled users; for this work, typically ensembles of approximately  $10^{487}\text{Rb}$  atoms at or below the BEC transition temperature  $T_c$  were provided in a tightly confining ‘atom chip’-style magnetic trap, although much hotter samples were also used. The facility-provided default trap, common to all users, was not suitable for shell-potential exploration owing to its high aspect ratio (about 10) and proximity to the atom-chip surface—effectively the wall of the vacuum chamber. We thus initiated all experiments with an expansion trajectory designed to bring the ultracold sample away from the vacuum wall and reduce the aspect ratio of its confining trap<sup>35,36</sup>. The resulting trap configuration served as an initial condition for these experiments, featuring an ensemble of ultracold  $^{87}\text{Rb}$  atoms, nominally in the  $|F = 2, m = 2\rangle$  internal state, confined in a trapping potential  $U_2(r)$  approximately 700  $\mu\text{m}$  from the surface of the CAL atom chip. The trap is described by an aspect ratio of about 3 and a geometric mean trapping frequency of  $\bar{\omega} = 2\pi \times 61(1)\text{Hz}$  (Methods). Turning on the coupling radiofrequency field (linearly polarized along  $z$ , the axis perpendicular to the atom chip) far below resonance projects the system into the appropriate dressed-state manifold—where the dressed state is nearly identical to the initial bare state—with further dynamic alteration occurring via ramps of  $\omega_{\text{rf}}$ . Typically, the frequency is referenced (via a detuning  $\Delta = \omega_{\text{rf}} - \omega_0$ ) to an experimentally determined ‘trap bottom’  $\omega_0$  defined such that  $\hbar\omega_0 = E_{2,2} - E_{2,1}$  (where  $\hbar$  is the reduced Planck constant), namely, the energy separation of the two topmost

states  $|F = 2, m = 2\rangle$  and  $|F = 2, m = 1\rangle$  in the  $F = 2$  ground state manifold. To move to a shell potential of chosen size, the value of  $\omega_{\text{rf}}$  is linearly ramped at a rate (typically about  $1\text{ kHz ms}^{-1}$ ) chosen for mechanical adiabaticity (Methods). After rapid (about  $1\text{--}10\ \mu\text{s}$ ) switching off of both the radiofrequency field and the magnetic trap, imaging of the resulting clouds is performed via destructive absorption imaging. The parameter space of the resulting datasets is spanned by variation of initial temperature  $T$ , atom number  $N$ , final detuning  $\Delta$  and the time of flight (TOF) between trap snap-off and imaging. Although the radiofrequency coupling strength ( $\Omega \propto B_{\text{rf}}$ ) can also alter the dressed-state trap geometry, for these experiments it was held constant at a value  $\Omega_0 = 2\pi \times 6(1)\text{ kHz}$ , calibrated via Rabi spectroscopy of the atomic clouds.

Figure 2 shows a variety of the ultracold shell structures that we have formed aboard CAL, including predictions of a semiclassical model whose potentials were initially developed in ref. <sup>24</sup>. In contrast to the idealized model of Fig. 1, these data represent structures consistent with an ellipsoidal shape caused by the 3:1 aspect ratio of the originating atom-chip magnetic trap. All images are absorption-imaging column densities; thus, all features are distorted compared with what tomographic techniques might reveal. Imaging resolution effects and the effects of shell-trap inhomogeneities also impact the visual character of the data. Residual potential-energy inhomogeneities in the shell potential are associated with (1) the decrease of the coupling radiofrequency amplitude with increasing distance from the antenna, (2) variation of the trap magnetic field direction and (3) the anharmonicity of the atom-chip magnetic trap. These are generally proportional to bubble size, and are predicted to be about  $\hbar \times 100\text{ Hz}$  ( $k_B \times 5\text{ nK}$ ; where  $\hbar$  and  $k_B$  are the Planck and Boltzmann constants, respectively) for roughly 100- $\mu\text{m}$ -size clouds, corresponding to effective gravitational effects of  $\lesssim 0.005\text{g}$ ; as such, residual microgravity accelerations of the ISS should not be relevant here. As such, given typical shell temperatures of the order of 100 nK, the visual leftward ( $-z$ ) bias of the shell structures is driven at moderate radii mostly through column-density distortion (the bubble is tilted in the  $x$ - $y$  plane) and at large radii mostly through the radiofrequency amplitude inhomogeneity. This interplay between trap shape, bubble size and inhomogeneities is illustrated through modelled shell-coverage maps in Fig. 2g, h, showing increasing leftward bias as the bubble size is increased. We note that the predicted thicknesses of either the condensate or the thermal shell clouds in these systems are in the range of about 1–10  $\mu\text{m}$ , as illustrated in Fig. 2e, k, revealing the ultracold-atom coverings of these bubble potentials to be remarkably delicate structures, which are impossible to generate in the presence of terrestrial gravity. For moderately sized bubbles as depicted in Fig. 2a–c and modelled in Fig. 2d–h, the modelled coverage

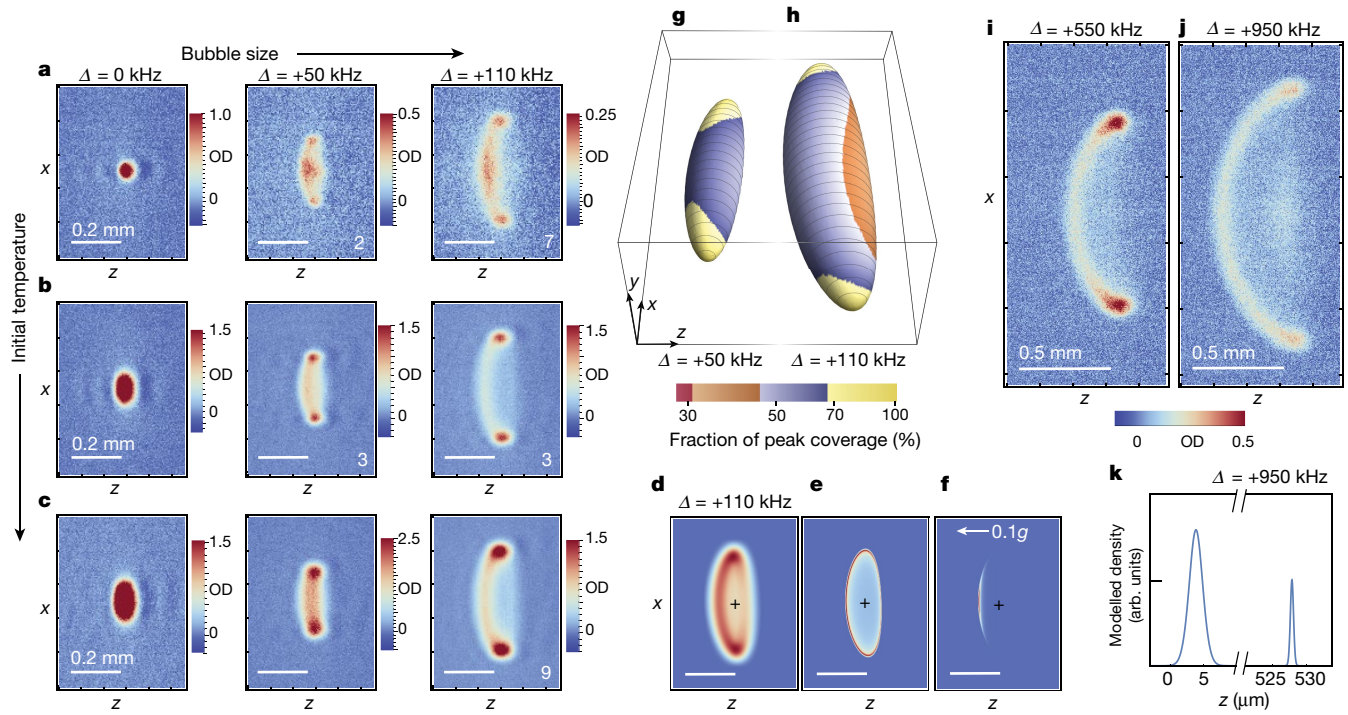


**Fig. 2 | Ultracold bubble observations and modelling.** **a**, Bubble inflation sequence with an initial temperature of about 100 nK (partially condensed) set by a radiofrequency knife value near 4.87 MHz; trap sizes are given by  $\Delta$  parameters of 0 kHz, +50 kHz and +110 kHz, respectively, left to right. All data show optical depth (OD); images were taken with minimal TOF expansion. **b**, Inflation sequence with initial temperature (about 300 nK) set by a radiofrequency knife value near 4.9 MHz. **c**, Inflation with initial temperature (about 400 nK) set by a radiofrequency knife value near 4.99 MHz. In all inflated clouds, note terrestrially unattainable lobes at  $\pm x$ . When present, the number in the bottom right corner denotes the number of images averaged together, originating in identical experimental sequences. **d**, Model prediction of the  $\Delta = +110$  kHz column density at  $T_{\text{bubble}} = 100$  nK, akin to the corresponding bubbles in **a–c**, where the model includes simple blurring by a point-spread function of width 40  $\mu\text{m}$ . **e**, The corresponding non-blurred model column

density. **f**, The model predictions of **e** modified by the presence of 10% of terrestrial gravity, demonstrating the impact of the microgravity environment. **g**, **h**, Illustrative model of bubble coverage for  $\Delta = +50$  kHz (**g**) and  $\Delta = +110$  kHz (**h**), both at typical bubble temperatures of 100 nK, showing an approximate factor-of-two variation around the bubble. It is noted that the larger bubble shows increased inhomogeneity, which corresponds to residual potential tilts of about 0.005g. **i**, **j**, Extreme inflation to millimetre-scale sizes with  $\Delta = +550$  kHz (**i**) and  $\Delta = +950$  kHz (**j**); the initial temperature (about 1  $\mu\text{K}$ ) is set by a radiofrequency knife value of 5.3 MHz. **k**, Model prediction of  $\Delta = +950$  kHz ensemble at  $T_{\text{bubble}} = 100$  nK; shown is a 1D slice along  $z$  of the predicted atomic density distribution. It is noted that the bubble-diameter-to-thickness ratio is about 500:1; also note that although the bubble coverage is suppressed at this  $\Delta$ , it remains discernible.

of the ultracold atomic film varies by less than a factor of two around the  $\Delta = 50$  kHz shell, and by a factor of three around the  $\Delta = 110$  kHz shell. In the limit of large  $\Delta$ , shells with a diameter on the few-millimetre scale are possible, as shown in Fig. 2i, j. The lobe structures seen in many images at the  $\pm x$  ends of the observed clouds are qualitatively observed in modelling through approximate imaging-resolution estimates, as shown in Fig. 2d. This stands in contrast to the associated modelling of perfect-resolution column density, shown in Fig. 2e, which de-emphasizes the lobe structure. At larger radii, this simple modelling does not suffice; a more sophisticated imaging analysis might yield deeper understanding here<sup>37</sup>.

## Bubble thermometry

In Fig. 3, we show the results of bubble thermometry with associated theoretical modelling of  $T_{\text{bubble}}(\Delta)$ . To provide a visual reference for the temperature relative to Bose–Einstein condensation, we also show  $T_c(\Delta)$  given typical values of atom number  $N$  for a given dataset. Thermometry is performed by turning off the trapping potential (radiofrequency and chip magnetic fields) and letting the cloud expand in TOF up to 48 ms, during which the atoms remain roughly centred around their original location given the weightless environment. The absorption profile (column density) of the cloud is then summed and fitted to standard profiles (Methods), which although less appropriate for

short TOF, yields a generally accurate impression of the initial size and long-TOF expansion speed of the released cloud. The key intuition for the thermodynamics of shell potentials is that the reshaping of the bare magnetic trap into a bubble trap of given radius is equivalent to an adiabatic expansion, albeit one not necessarily proceeding at constant phase-space density<sup>38</sup>. We show thermometry curves for samples initially partially condensed (Fig. 3d) as well as for samples with initial temperatures up to  $>3T_c$ , shown in Fig. 3a–c. For all four initial sample temperatures, we observe large drops in temperature as the bubble size is increased, with the most rapid change occurring over the range of  $\Delta$  associated with the atomic cloud hollowing out (as the trapping potential changes from harmonic to shell like).

To model these data, we developed estimates for temperatures of ultracold shells using a semiclassical fixed-entropy approach, with the entropy associated with a given theory curve in Fig. 3 set by the initial temperature and number in the given configuration (Methods). This model does not include interatomic interactions, which have little impact given the low atomic density of the samples spread across the majority of a shell. Although this modelling approach for  $T_{\text{bubble}}(\Delta)$  yields good agreement for the hottest initial sample in Fig. 3a, the data increasingly show suppressed cooling effects at lower initial temperatures, despite directional agreement. We attribute these discrepancies, most significantly shown in Fig. 3d, to a combination of several possible factors. A primary factor could be violations of mechanical adiabaticity

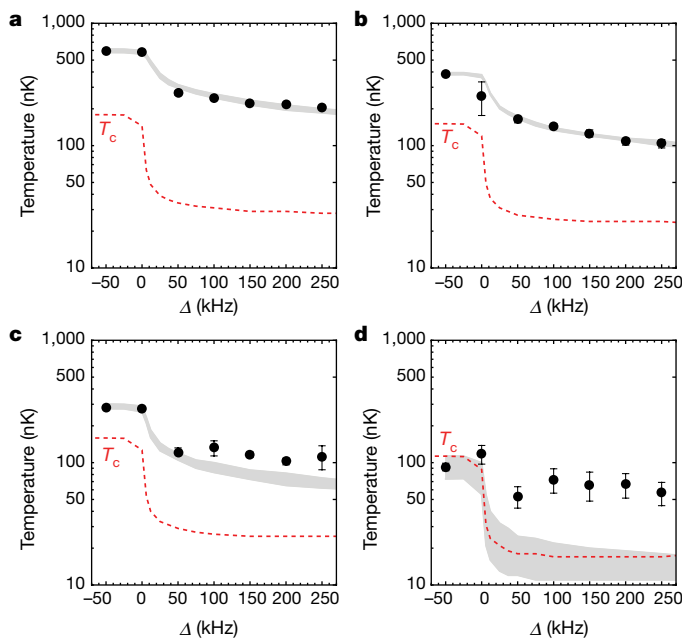


**Fig. 3 | Thermometry of bubbles.** **a–d**,  $T_{\text{bubble}}(\Delta)$  data (black), where the detuning  $\Delta$  serves as a proxy for bubble size, and with inflation from the bare harmonic trap beginning roughly around  $\Delta = 0$ . Error bars (where visible) and uncertainties represent standard errors unless otherwise stated. Also shown are theoretical  $T_{\text{bubble}}(\Delta)$  (grey) and  $T_c(\Delta)$  (dashed) predictions for initial pre-inflation temperatures set by evaporative-cooling radiofrequency knife values, as follows: 600(20) nK (5.1 MHz) (**a**), 390(10) nK (5.0 MHz) (**b**), 290(10) nK (4.93 MHz) (**c**) and 90(20, 99% confidence interval) nK (4.855 MHz) (**d**), where the last initial condition is a partial BEC, although clouds appear thermal for all positive  $\Delta$ . Theory curves for  $T_c(\Delta)$  (dashed) are shown for illustrative purposes and assume a typical mean atom number of  $200(10) \times 10^3$ ,  $120(5) \times 10^3$ ,  $140(5) \times 10^3$  and  $50(5) \times 10^3$  for **a–d**, respectively. The data show significant cooling as the bubble trap is inflated from an unperturbed initial harmonic trap.

associated with the technical quality of the inflation ramp, particularly owing to radiofrequency phase-coherence and step-size factors<sup>39</sup>. Another factor could be potential systematic experimental errors in thermometry at low temperatures, including effects owing to a faint absorption signal. Another could be the failure of the semiclassical approximation associated with the transition to quasi-2D confinement, but recent work by many of the current authors<sup>40</sup> found that an idealized spherically symmetric bubble trap-confined condensate gives slightly lower predictions for  $T_{\text{bubble}}(\Delta)$ . A more fundamental source could be in the breakdown of adiabaticity in the inflationary process, specifically in regimes close to the hollowing-out detuning (where the trapping potential briefly looks quartic) and near the critical temperature  $T_c$ , where fluctuations abound. Here, the intrinsic relaxational timescale of the system tends to diverge, throwing the system out of equilibrium even for slow tuning<sup>41</sup>. Regarding 2D confinement, we predict confining trap frequencies (varying around the bubble) in the range of 200–400 Hz for small ( $\Delta = +50$  kHz) bubbles and in the range of 400–1,000 Hz for large ( $\Delta = +250$  kHz) bubbles, implying a general requirement that bubble temperatures be significantly below  $h/k_B \times 1,000$  Hz = 50 nK for even sporadic 2D confinement to occur.

A key feature of bubble thermodynamics is that while the calculated and observed  $T_{\text{bubble}}(\Delta)$  drops precipitously as the trapping potential is adiabatically ‘inflated’, the calculated  $T_c$  for a given  $N$  does not drop commensurately. This is caused by an initial drop in phase-space density even at constant entropy; this decoupling of phase-space density and entropy owing to geometrical changes has been exploited in various cold-atom experiments<sup>42–44</sup> but in shell geometry it presents an added challenge. Thus, we find in principle that an initially barely condensed cloud (such as used in Fig. 3d) should enter the normal phase again on inflation, even given perfect adiabaticity, and potentially re-condense on extreme inflation. This issue (and the thermodynamics of shell inflation in general, including the nature, role and limits of the semiclassical approximation) is discussed comprehensively in ref.<sup>40</sup>.

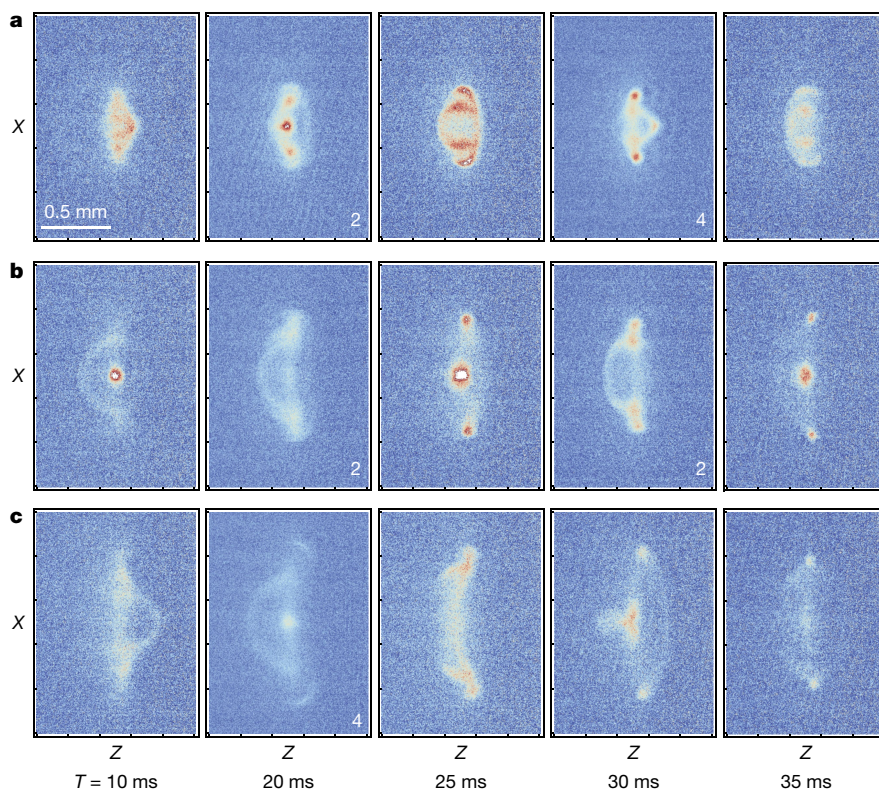


**Fig. 4 | Evolution on removal of dressing.** **a–c**, Rapidly turning off the radiofrequency field forces evolution in the bare magnetic trap according to the projected spin component. Red corresponds to relatively higher optical depth; blue, to lower. The rows correspond to three different shell sizes: dressing detuning  $\Delta = 150$  kHz (**a**),  $\Delta = 350$  kHz (**b**) and  $\Delta = 550$  kHz (**c**). Evolution time  $t$  increases rightwards as denoted at the bottom. When present, the number in the lower right corner denotes the number of images averaged together, originating in identical experimental sequences. The qualitative recurrence timescale of 10 ms is noted, which roughly corresponds to the trap oscillation period in the horizontal direction.

## Trapped bubble propagation

Given a dressed (spin superposition) ultracold shell system, an immediate point of curiosity arises regarding what might happen on removal of the dressing field while preserving the confining magnetic trap. Such an action should (in the limit of rapid turn-off) project the dressed bubble eigenstate into its bare spin components, which would then experience the original magnetic trap as dictated by the magnetic moment of those components. Thus, we would expect an inward-propagating shell to appear as the hold time  $t$  in the ‘de-dressed’ trap is varied. In Fig. 4, we show example observations of such propagation of (probably thermal) shell ensembles. Understanding of the qualitative nature of this effect is an important prologue to understanding the behaviour of dressed condensates undergoing similar propagation, which should result in complex interference patterns given by time evolution of the bare ground-state spin components<sup>13</sup>; it also suggests future investigations along the lines of the ‘Bose nova’ collapse experiments<sup>45</sup>.

## Conclusion and outlook

We have observed and characterized ultracold bubble systems and established a model and theoretical framework for them. The capacity to perform these experiments is at present unique to laboratories operating in a microgravity environment, and our observations point the way to future work aiming to reach the condensed bubble state and exploring its fundamental nature. With significantly lower initial temperatures in future experiments, with concomitant improvements in condensate fraction, adiabatic inflation would not provoke such significant loss of the condensate fraction. Initial condensate fraction improvements can occur through better-engineered expansion paths from the default CAL trap to our starting trap, and radiofrequency-dressing improvements are feasible through technical changes to the experimental hardware and software aboard CAL. This has been initiated by a recent hardware upgrade, including a larger radiofrequency antenna with associated increase in dressing homogeneity; this should also improve adiabaticity and bubble quality, as could the use of compensatory microwave dressing<sup>46,47</sup>. Alternatively, planned facilities such as the Bose–Einstein Condensate and Cold Atom Lab (BECCAL)<sup>48</sup> could incorporate secondary evaporative cooling of the dressed clouds<sup>49</sup>, permitting a direct path to a higher condensate fraction.

Future work (on CAL or successors) could generate vortices in condensate bubbles either through direct stirring or rotation of the dressed trap, or through spontaneous generation of vortices across the condensate phase transition through the Kibble–Zurek mechanism. Experimental exploration of recent theoretical work regarding the role of the Berezinskii–Kosterlitz–Thouless transition in 2D superfluid bubbles would be a compelling target as a case of the general problem of quantum-gas physics on curved manifolds<sup>78,50</sup>. In addition, multi-axis imaging for complete characterization of the bubble structure should be possible, and implementation of multi-radiofrequency protocols for nested (tunnelling) shells is within sight<sup>51,52</sup>, as are experiments aiming at observation of BEC collective modes that are unique to hollow condensates. Given the establishment of these techniques, bubble inflation (up to and beyond the few-millimetre scale) could drive ‘model universe’ experiments<sup>20</sup>, the fundamental limits of inflation adiabaticity and quantum behaviour at dilute-BEC extremes could be explored—potentially with multiple species<sup>53,54</sup>—and bubble cooling and shaping techniques could be applied to spaceborne quantum sensing protocols<sup>55</sup>.

## Online content

Any methods, additional references, Nature Research reporting summaries, source data, extended data, supplementary information,

acknowledgements, peer review information; details of author contributions and competing interests; and statements of data and code availability are available at <https://doi.org/10.1038/s41586-022-04639-8>.

- Hadzibabic, Z., Kruger, P., Cheneau, M., Battelier, B. & Dalibard, J. Berezinskii–Kosterlitz–Thouless crossover in a trapped atomic gas. *Nature* **441**, 1118–1121 (2006).
- Cladé, P., Ryu, C., Ramanathan, A., Helmerson, K. & Phillips, W. D. Observation of a 2D Bose gas: from thermal to quasicondensates to superfluid. *Phys. Rev. Lett.* **102**, 170401 (2009).
- Kinoshita, T., Wenger, T. & Weiss, D. S. Observation of a one-dimensional Tonks–Girardeau gas. *Science* **305**, 1125–1128 (2004).
- Paredes, B. et al. Tonks–Girardeau gas of ultracold atoms in an optical lattice. *Nature* **429**, 277–281 (2004).
- Eckel, S. et al. Hysteresis in a quantized superfluid ‘atomtronic’ circuit. *Nature* **506**, 200–203 (2014).
- Chin, C., Grimm, R., Julienne, P. & Tiesinga, E. Feshbach resonances in ultracold gases. *Rev. Mod. Phys.* **82**, 1225–1286 (2010).
- Tononi, A., Pelster, A. & Salasnich, L. Topological superfluid transition in bubble-trapped condensates. *Phys. Rev. Res.* **4**, 013122 (2022).
- Tononi, A., Cinti, F. & Salasnich, L. Quantum bubbles in microgravity. *Phys. Rev. Lett.* **125**, 010402 (2020).
- Tononi, A. & Salasnich, L. Bose–Einstein condensation on the surface of a sphere. *Phys. Rev. Lett.* **123**, 160403 (2019).
- Padavić, K., Sun, K., Lannert, C. & Vishveshwara, S. Vortex–antivortex physics in shell-shaped Bose–Einstein condensates. *Phys. Rev. A* **102**, 043305 (2020).
- Sun, K., Padavić, K., Yang, F., Vishveshwara, S. & Lannert, C. Static and dynamic properties of shell-shaped condensates. *Phys. Rev. A* **98**, 013609 (2018).
- Padavić, K., Sun, K., Lannert, C. & Vishveshwara, S. Physics of hollow Bose–Einstein condensates. *Europhys. Lett.* **120**, 20004 (2017).
- Lannert, C., Wei, T. C. & Vishveshwara, S. Dynamics of condensate shells: collective modes and expansion. *Phys. Rev. A* **75**, 013611 (2007).
- Möller, N. S., Santos, F. E. Ad, Bagnato, V. S. & Pelster, A. Bose–Einstein condensation on curved manifolds. *New J. Phys.* **22**, 063059 (2020).
- Bereta, S. J., Caracanhas, M. A. & Fetter, A. L. Superfluid vortex dynamics on a spherical film. *Phys. Rev. A* **103**, 053306 (2021).
- Zhang, J. & Ho, T.-L. Potential scattering on a spherical surface. *J. Phys. B* **51**, 115301 (2018).
- Mitra, K., Williams, C. J. & Sá de Melo, C. A. R. Superfluid and Mott-insulating shells of bosons in harmonically confined optical lattices. *Phys. Rev. A* **77**, 033607 (2008).
- Banik, S. et al. Accurate determination of Hubble attenuation and amplification in expanding and contracting cold-atom universes. *Phys. Rev. Lett.* **128**, 090401 (2022).
- Bhardwaj, A., Vaido, D. & Sheehy, D. E. Inflationary dynamics and particle production in a toroidal Bose–Einstein condensate. *Phys. Rev. A* **103**, 023322 (2021).
- Eckel, S., Kumar, A., Jacobson, T., Spielman, I. B. & Campbell, G. K. A rapidly expanding Bose–Einstein condensate: an expanding universe in the lab. *Phys. Rev. X* **8**, 021021 (2018).
- Aveline, D. C. et al. Observation of Bose–Einstein condensates in an Earth-orbiting research lab. *Nature* **582**, 193–197 (2020).
- Zobay, O. & Garraway, B. M. Two-dimensional atom trapping in field-induced adiabatic potentials. *Phys. Rev. Lett.* **86**, 1195–1198 (2001).
- Elliott, E. R., Krutzik, M. C., Williams, J. R., Thompson, R. J. & Aveline, D. C. NASA’s Cold Atom Lab (CAL): system development and ground test status. *npj Microgravity* **4**, 16 (2018).
- Lundblad, N. et al. Shell potentials for microgravity Bose–Einstein condensates. *npj Microgravity* **5**, 30 (2019).
- Zobay, O. & Garraway, B. M. Properties of coherent matter-wave bubbles. *Acta Phys. Slovaca* **50**, 359–368 (2000).
- Zobay, O. & Garraway, B. Atom trapping and two-dimensional Bose–Einstein condensates in field-induced adiabatic potentials. *Phys. Rev. A* **69**, 023605 (2004).
- Perrin, H. & Garraway, B. M. Trapping atoms with radio frequency adiabatic potentials. *Adv. At. Mol. Opt. Phys.* **66**, 181–262 (2017).
- Garraway, B. M. & Perrin, H. Recent developments in trapping and manipulation of atoms with adiabatic potentials. *J. Phys. B* **49**, 172001 (2016).
- White, M., Gao, H., Pasienski, M. & DeMarco, B. Bose–Einstein condensates in rf-dressed adiabatic potentials. *Phys. Rev. A* **74**, 023616 (2006).
- Merloti, K. et al. A two-dimensional quantum gas in a magnetic trap. *New J. Phys.* **15**, 033007 (2013).
- Colombe, Y. et al. Ultracold atoms confined in rf-induced two-dimensional trapping potentials. *Europhys. Lett.* **67**, 593–599 (2004).
- Shibata, K., Ikeda, H., Suzuki, R. & Hirano, T. Compensation of gravity on cold atoms by a linear optical potential. *Phys. Rev. Res.* **2**, 013068 (2020).
- Guo, Y. et al. An annular quantum gas induced by dimensional reduction on a shell. Preprint at <https://arxiv.org/abs/2105.12981> (2021).
- Meister, M., Roura, A., Rasel, E. M. & Schleich, W. P. The space atom laser: an isotropic source for ultra-cold atoms in microgravity. *New J. Phys.* **21**, 013039 (2019).
- Sackett, C. A., Lam, T. C., Stickney, J. C. & Burke, J. H. Extreme adiabatic expansion in micro-gravity: modeling for the Cold Atomic Laboratory. *Microgravity Sci. Technol.* **30**, 155–163 (2017).
- Pollard, A. R., Moan, E. R., Sackett, C. A., Elliott, E. R. & Thompson, R. J. Quasi-adiabatic external state preparation of ultracold atoms in microgravity. *Microgravity Sci. Technol.* **32**, 1175–1184 (2020).
- Putra, A., Campbell, D. L., Price, R. M., De, S. & Spielman, I. B. Optimally focused cold atom systems obtained using density–density correlations. *Rev. Sci. Instrum.* **85**, 013110 (2014).
- Pinkse, P. W. H. et al. Adiabatically changing the phase-space density of a trapped Bose gas. *Phys. Rev. Lett.* **78**, 990–993 (1997).

39. Morizot, O. et al. Influence of the radio-frequency source properties on RF-based atom traps. *Eur. Phys. J. D* **47**, 209–214 (2008).
40. Rhyno, B., Lundblad, N., Aveline, D. C., Lannert, C. & Vishveshwara, S. Thermodynamics in expanding shell-shaped Bose–Einstein condensates. *Phys. Rev. A* **104**, 063310 (2021).
41. Dzarmaga, J. Dynamics of a quantum phase transition and relaxation to a steady state. *Adv. Phys.* **59**, 1063–1189 (2010).
42. Lin, Y.-J., Perry, A., Compton, R., Spielman, I. & Porto, J. Rapid production of  $^{87}\text{Rb}$  Bose–Einstein condensates in a combined magnetic and optical potential. *Phys. Rev. A* **79**, 063631 (2009).
43. Stamper-Kurn, D. M. et al. Reversible formation of a Bose–Einstein condensate. *Phys. Rev. Lett.* **81**, 2194–2197 (1998).
44. Weber, T., Herbig, J., Mark, M., Nagerl, H.-C. & Grimm, R. Bose–Einstein condensation of cesium. *Science* **299**, 232–235 (2003).
45. Roberts, J. L. et al. Controlled collapse of a Bose–Einstein condensate. *Phys. Rev. Lett.* **86**, 4211–4214 (2001).
46. Sinuco-Leon, G. A. et al. Microwave spectroscopy of radio-frequency-dressed Rb87. *Phys. Rev. A* **100**, 053416 (2019).
47. Fancher, C. T., Pyle, A. J., Rotunno, A. P. & Aubin, S. Microwave ac Zeeman force for ultracold atoms. *Phys. Rev. A* **97**, 043430 (2018).
48. Frye, K. et al. The Bose–Einstein Condensate and Cold Atom Laboratory. *EPJ Quantum Technol.* **8**, 1 (2021).
49. Alzar, C. G., Perrin, H., Garraway, B. & Lorent, V. Evaporative cooling in a radio-frequency trap. *Phys. Rev. A* **74**, 053413 (2006).
50. Caracanhas, M. A., Massignan, P. & Fetter, A. L. Superfluid vortex dynamics on an ellipsoid and other surfaces of revolution. *Phys. Rev. A* **105**, 023307 (2022).
51. Luksch, K. et al. Probing multiple-frequency atom–photon interactions with ultracold atoms. *New J. Phys.* **21**, 073067 (2019).
52. Harte, T. L. et al. Ultracold atoms in multiple radio-frequency dressed adiabatic potentials. *Phys. Rev. A* **97**, 013616 (2018).
53. Wolf, A. et al. Shell-shaped Bose–Einstein condensates realized with dual-species mixtures. Preprint at <https://arxiv.org/abs/2110.15247> (2021).
54. Andriati, A., Brito, L., Tomio, L. & Gammal, A. Stability of a Bose-condensed mixture on a bubble trap. *Phys. Rev. A* **104**, 033318 (2021).
55. Lachmann, M. D. et al. Ultracold atom interferometry in space. *Nat. Commun.* **12**, 1317 (2021).

**Publisher's note** Springer Nature remains neutral with regard to jurisdictional claims in published maps and institutional affiliations.

© The Author(s), under exclusive licence to Springer Nature Limited 2022

## Methods

### User facility and sample preparation

CAL is a multi-user research facility installed and operating aboard the ISS, where it has been running cold-atom experiments on a daily basis since June 2018. Remotely controlled from the Jet Propulsion Laboratory (JPL) in Pasadena, California, the instrument produces  $^{87}\text{Rb}$  BECs using an atom-chip device and carries a suite of tools that enable a variety of cold-atom studies led by multiple investigators from around the world. The BEC production is based on laser-cooled atoms that are subsequently magnetically trapped and transported to an atom-chip surface, where they are cooled via forced evaporation with radiofrequency radiation. For use with the experiments associated with this work, the trapped sample was transported away from the chip in a process that reduced the needle-like aspect ratio of the original trap, and reduced the overall trap tightness. Done rapidly and/or with simple linear ramps of trap parameters, this process could result in significant centre-of-mass excitation rendering further work difficult; to ameliorate this, we applied custom expansion pathways on the basis of the formalism developed in ref. <sup>35</sup> and observed that with sufficiently large overall expansion time, the residual trap motion could be reduced to  $\lesssim 1\text{ }\mu\text{m}$ . Deliberately rapid expansion pathways were used to excite measurable ‘sloshing’, which was used to confirm our modelling of the chip trap system. We denote the trapping frequencies as  $\omega_i$  ( $i = 1, 2, 3$ ), where the principal oscillation direction associated with  $\omega_1$  and  $\omega_2$  lies in the  $x$ - $y$  plane parallel to the atom chip, and that of  $\omega_3$  lies in the  $z$  direction (perpendicular to the chip). Observations of  $\omega_3$  yielded a best estimate of  $2\pi \times 100(1)$  Hz, consistent with our model prediction of 101 Hz; model predictions for the other frequencies were  $\omega_1 = 2\pi \times 31$  Hz and  $\omega_2 = 2\pi \times 98$  Hz. Residual micromotion remaining from the sample expansion trajectory was estimated to be of characteristic amplitude  $< 1\text{ }\mu\text{m}$ .

### Imaging

Measurement of the atom-cloud density distribution was carried out using absorption imaging techniques with an optical path passing parallel to the chip surface (along the instrument’s  $y$  axis). The optical beam was approximately 10 mm in diameter and centred about 4 mm below the chip surface, and was directed via collection optics into a complementary metal–oxide–semiconductor camera with an associated magnification factor of 1.2. A small magnetic field was applied along the  $y$  axis to enhance the absorption with this circularly polarized optical beam. The results reported here were collected using two 40- $\mu\text{s}$  pulses separated by 53 ms, with the first pulse containing atoms and the second serving as a reference. The effective pixel size used for all analysis in this paper is  $\ell = 4.52\text{ }\mu\text{m}$ .

### Thermometry

Thermometry proceeded via the standard technique of TOF expansion, whereby the long-TOF size of the cloud is indicative of the temperature of the sample before its release. The starting point for the data from CAL was an optical depth image  $\text{OD}(x_j, z_i)$ , restricted for the purposes of thermometry to a small window in the vicinity of the observed atomic cloud. Thermometry was performed via Gaussian (or Gaussian + Thomas–Fermi) fits to 1D arrays  $g(z_i) = \sum_j \text{OD}(x_j, z_i)$ , which yielded Gaussian widths  $\sigma(\tau)$  (for TOF value  $\tau$ ) and (if appropriate) condensate fraction. Although for dressed clouds such as the short-TOF shells in Fig. 2a–c this Gaussian width is not inherently meaningful beyond providing root-mean-square size information, it serves to constrain the initial size and our modelling indicates that it does not distort the thermometry. For a given TOF expansion, the temperature is obtained by fitting the cloud-size data to the TOF-convolved width  $\sigma(\tau) = \sqrt{\sigma(0)^2 + (k_B T/M)\tau^2}$  where  $M$  is the  $^{87}\text{Rb}$  atomic mass. For images where shells had not yet formed (that is,  $\Delta \leq 50$  kHz) and starting temperatures were such that a

BEC was present, a hybrid fit was used to extract the condensate information. For the partially condensed samples in Fig. 3d, condensate fractions of 10(5)% were observed. The short (2.6 ms) TOF widths of uninflated partially condensed clouds were limited by imaging resolution, and for thermometry were conservatively estimated to be 10(5)  $\mu\text{m}$ . The results of all fits associated with Fig. 3 are shown in Extended Data Fig. 1.

A complicating factor for most image analyses (and especially for the coldest samples) was the presence of a background halo of atoms in the  $|2, 0\rangle$  state resulting from the evaporative cooling used to generate our initial conditions. This halo was observed and analysed in detail by the CAL mission<sup>21</sup> and is a unique feature to microgravity BEC creation, as in terrestrial experiments the very weakly trapped halo atoms would be removed by gravity. For our purposes, these atoms present an additional component to all datasets that is difficult to separately fit and remove, as for most shell clouds the size is comparable. Fortunately, however, the halo cloud is slightly displaced in  $z$  from our bubble clouds, and as such the fitting window can be biased to ignore approximately half the halo such that its impact is lessened while preserving small-TOF shell structure, as shown in Extended Data Fig. 2. Nevertheless, the halo presence probably adds systematic uncertainty to both low-temperature thermometry and (when appropriate) condensate fraction.

### Thermodynamic model

Here we summarize our modelling approach for predicting thermometry in the shell geometries at hand. We consider two aspects, namely, (1) the transition temperature  $T_c$  at which we expect a fraction of condensate to appear for a given shell-shaped geometry and (2) the change in temperature of the ultracold atomic gas as the trapping potential evolves and gives rise to adiabatic expansion.

At temperatures much larger than the single-particle energy-level spacing, one can employ a semiclassical approximation<sup>56,57</sup>. For a collection of non-interacting  $^{87}\text{Rb}$  atoms, this amounts to using the energy relation  $\mathbf{p}^2/2M + U(\mathbf{r})$  where  $M$ ,  $\mathbf{p}$  and  $U(\mathbf{r})$  are the particle’s mass, momentum and confining potential, respectively. Note that interaction effects have been disregarded here due to the low particle density present in the experimental bubbles.

The validity of the semiclassical approximation for shell-shaped potentials is discussed towards the end of this section and is addressed in more detail in ref. <sup>40</sup>. In this scheme, standard thermodynamic sums over eigenstates of the Schrödinger equation are replaced by integrals over position and momentum<sup>56,57</sup>. The momentum integrals can be performed analytically; for instance, one finds that the single-particle density of states takes the form

$$\rho(\varepsilon) = \frac{2}{\sqrt{\pi}} \left( \frac{M}{2\pi\hbar^2} \right)^{3/2} \int d\mathbf{r} \theta(\varepsilon - U(\mathbf{r})) \sqrt{\varepsilon - U(\mathbf{r})}, \quad (1)$$

where the integration is over all space,  $\varepsilon$  is energy, and  $\theta(\cdot)$  denotes the Heaviside step function<sup>58</sup>. To carry out spatial integrals, we employ a numeric method. We create a spatial grid with typical lattice spacing 1  $\mu\text{m}$  and apply the numerically generated potential  $U(\mathbf{r})$ .

As discussed in the main text, the dressed potentials of interest are characterized by a detuning frequency  $\Delta$ , which, when increased, inflates the size of the bubble. As a function of detuning, we use the semiclassical formalism to numerically calculate both the transition temperature,  $T_c(\Delta)$ , and the temperature of the gas during adiabatic expansions,  $T_{\text{bubble}}(\Delta)$  given an initial temperature. In the thermodynamic limit, the transition temperature  $T_c(\Delta)$  is found in the semiclassical approximation by setting the chemical potential equal to the minimum value of  $U(\mathbf{r})$  (which we set to zero here for convenience) and finding the temperature that makes the number of excited particles equal to the total number of particles. Explicitly, for each dressed potential, we determine the temperature that satisfies the equation

$$N = \int d\varepsilon \rho(\varepsilon) \frac{1}{e^{\varepsilon/k_B T_c} - 1}. \quad (2)$$

Alternatively, by inserting equation (1) and integrating over energy, this process could be performed using the following<sup>59</sup>:

$$N = \frac{1}{\Lambda_{\text{th}}^3} \int d\mathbf{r} g_{3/2}[e^{-U(\mathbf{r})/k_B T_c}], \quad (3)$$

where  $\Lambda_{\text{th}} = \sqrt{2\pi\hbar^2/Mk_B T}$  is the thermal de Broglie wavelength (evaluated at  $T_c$ ) and  $g_s[z] = \sum_{n=1}^{\infty} z^n/n^s$  is the Bose function of index  $s$  and argument  $z$ .

Turning to adiabatic expansion modelling, we first fix the number of particles in our trap  $N$  and the initial temperature of the system before expansion, that is, when the trap potential is at its lowest detuning frequency. Next, we find the entropy associated with this initial setup. This is done numerically by simultaneously solving the equations for particle number  $N$  and entropy  $S$ :

$$N = N_0 + \int d\varepsilon \rho(\varepsilon) f(\varepsilon), \quad (4a)$$

$$S = k_B \int d\varepsilon \rho(\varepsilon) \{[1+f(\varepsilon)] \ln [1+f(\varepsilon)] - f(\varepsilon) \ln f(\varepsilon)\}, \quad (4b)$$

where  $N_0$  is the number of condensed particles and  $f(\varepsilon) = \{\exp[(\varepsilon - \mu)/k_B T] - 1\}^{-1}$  is the Bose–Einstein distribution function at temperature  $T$  and chemical potential  $\mu$ . Whereas below  $T_c$  we have  $\mu = 0$ , above  $T_c$ , where  $N_0 = 0$ , we must determine the chemical potential. As in the calculation of  $T_c$ , one can carry out the energy integration to obtain convenient formulae for both the particle number and the entropy ( $S$ ) of a trapped Bose gas<sup>59</sup>:

$$N = N_0 + \frac{1}{\Lambda_{\text{th}}^3} \int d\mathbf{r} g_{3/2}[z(\mathbf{r})], \quad (5a)$$

$$S = \frac{k_B}{\Lambda_{\text{th}}^3} \int d\mathbf{r} \left\{ \frac{5}{2} g_{5/2}[z(\mathbf{r})] - g_{3/2}[z(\mathbf{r})] \ln z(\mathbf{r}) \right\}, \quad (5b)$$

where  $z(\mathbf{r})$  is the local fugacity  $\exp[(\mu - U(\mathbf{r}))/k_B T]$ .

Once an initial entropy is known, the evolution of the temperature during expansion can be determined. We increase  $\Delta$  (considering a different dressed potential) and find the new temperature of the gas by simultaneously demanding both the semiclassical expressions for the total particle number and entropy above remain fixed. Holding the entropy constant is equivalent to demanding adiabaticity during the expansion. The results obtained using these methods are shown and discussed in the main text. The uncertainty bands on the theory curves for  $T_c(\Delta)$  in Fig. 3 are approximately  $\pm 10$  nK (originating in the spread of  $N$  in a given dataset) and do not affect any interpretation of this work.

The semiclassical formulae outlined above are useful as they can be applied to arbitrary 3D potentials. However, the expressions were found by treating momentum as continuous. This assumes that all spatial dimensions of the system are large, but as the bubble expands it becomes tightly confined radially. As discussed in ref.<sup>40</sup>, when compared with semiclassical results, quantum mechanical modelling of a radially symmetric bubble shows a decrease in the predicted critical temperature at large detuning along with relatively minor changes in the temperature predicted during adiabatic expansions.

If we consider an idealized fully 2D spherical bubble of radius  $R$ , the single-particle energy spectrum,  $\hbar^2 l(l+1)/(2MR^2)$ , is characterized by its angular momentum  $l = 0, 1, 2, \dots$  and has degeneracy  $(2l+1)$ . For temperatures much larger than the level spacing, sums over angular momentum can be replaced with integrals and analytic results for various thermodynamic quantities can be obtained<sup>9</sup>. For a fixed particle

number, one finds in either the normal or condensed phase that the entropy is a function of the dimensionless quantity  $MR^2 k_B T/\hbar^2$  and hence (fixed entropy) adiabatic expansions require  $T \propto 1/R^2$ . For a spherically symmetric bubble trap, at large radii the square of the radius should scale with the detuning frequency<sup>40</sup>; thus, for a large, thin bubble we expect the temperature during adiabatic expansions to scale as  $T \propto 1/\Delta$ .

## Dressing Hamiltonian

Below is the dressing Hamiltonian that was used for all our modelling, developed through application of a rotating frame and the rotating-wave approximation.

$$\mathcal{H} = \begin{pmatrix} 2\omega & \Omega/2 & 0 & 0 & 0 \\ \Omega/2 & \omega & \sqrt{\frac{3}{2}}\Omega/2 & 0 & 0 \\ 0 & \sqrt{\frac{3}{2}}\Omega/2 & 0 & \sqrt{\frac{3}{2}}\Omega/2 & 0 \\ 0 & 0 & \sqrt{\frac{3}{2}}\Omega/2 & -\omega & \Omega/2 \\ 0 & 0 & 0 & \Omega/2 & -2\omega \end{pmatrix} + \mathcal{H}_{\text{Zeeman}}(\mathbf{r}) \quad (6)$$

where  $\mathcal{H}_{\text{Zeeman}}(\mathbf{r})$  is diagonal and represents the (exact) Zeeman shifts of the states in use, which for this work are those in the <sup>87</sup>Rb upper hyperfine ground-state manifold denoted by  $|F=2, m_F\rangle$ , with  $m_F$  taking values from  $-2$  to  $2$ . Use of this Hamiltonian assumes that the coupling strength (set in this case by the Rabi frequency  $\Omega$ ) is always and everywhere sufficiently large to ensure dressing adiabaticity, thus ensuring the stability of atoms in a given  $m'$  state, protected against ‘Landau–Zener’ losses to lower-lying dressed spin states<sup>60</sup>. Our typical operating parameter of  $\Omega/2\pi = 6(1)$  kHz is consistent with lifetimes exceeding 150 ms, confirmed by hold-time measurements showing no significant loss. These observations were performed with final radiofrequency knife values of 5.00 MHz and 4.86 MHz and performed at  $\Delta \simeq +110$  kHz. Given a driving frequency  $\omega$  with coupling strength  $\Omega(\mathbf{r})$ , we calculate the dressed potentials  $U_{m'}^*(\mathbf{r})$  as the spatially dependent eigenvalues of  $\mathcal{H}$ . These potentials can be approximately expressed as proportional to  $\sqrt{\delta(\mathbf{r})^2 + \Omega(\mathbf{r})^2}$ , where  $\delta(\mathbf{r})$  is the difference between the driving radiofrequency and the local Larmor frequency. Although not of specific interest in this work, the eigenvectors of  $\mathcal{H}$  represent the decomposition of the dressed spin state of an atom at  $\mathbf{r}$  into the lab-spin basis. Accounting for terrestrial gravitational effects would require the addition of an  $Mgz$ -like term to the Hamiltonian. Inhomogeneities in the magnitude and direction of  $\Omega$  result in effective gravitational tilts to the dressed potentials, discussed thoroughly in ref.<sup>24</sup>.

## Rabi calibration

A crucial parameter in the observation and modelling of ultracold radiofrequency-dressed systems is the coupling strength  $\Omega$ . In our case, it is driven by the interaction between the atoms and a radiofrequency field originating in a nearby wire loop. In general, the coupling strength is state dependent and spatially dependent owing to the inhomogeneous amplitude and direction of  $\mathbf{B}_{\text{rf}}$ , and frequency dependent owing to the nature of the radiofrequency amplifier and coil design. Nevertheless, a single parameter is used as a basis for our modelling, with various inhomogeneities accounted for separately in the model. We obtained a coupling parameter  $\Omega/2\pi$ —the Rabi frequency—using five-level Rabi spectroscopy of the  $F=2$  manifold. This was performed by preparing an ultracold sample in the  $|2, 2\rangle$  state in a trapping configuration relaxed from the initial tight trap. We then switched off the trapping fields, maintaining a constant bias field of approximately 5.2 G. After a radiofrequency pulse of 100  $\mu$ s duration and variable frequency near 3.7 MHz, a Stern–Gerlach gradient was applied to separate differing spin components, followed by conventional absorption imaging. The resulting five-level Rabi spectra were

fit using optimization routines (Mathematica 12.3) resulting in a conservative estimate of  $\Omega/2\pi = 6(1)$  kHz (at this radiofrequency) and an estimate of the constant bias field of  $5.238(1)$  G, with uncertainty largely coming from shot-to-shot noise in the spin populations combined with imaging noise. A separate effort taken by JPL/CAL researchers found a slightly higher Rabi frequency of about 8 kHz near 27 MHz, suggesting general broadband capability of the radiofrequency amplifier. The data taken in this paper generally were taken with radiofrequencies in the 2–3 MHz range, depending on initial and final shell inflation parameters.

### Details of the radiofrequency ramp

The radiofrequency radiation is generated by an AWG (National Instruments model PXI 5422), amplified and emitted from a double loop ( $OD \approx 10$  mm) of copper wire located on the ambient side of the atom chip. This radiofrequency source is used for evaporative cooling and (specifically for this work) applied with low-to-high sweeps of frequency to dress the cold-atom traps. The rapidity of a frequency sweep is an influential parameter for maintaining adiabaticity in bubble inflation, both for the dressed potentials themselves (spin-following adiabaticity) and the mechanical adiabaticity associated with the deformation of the dressed trap potentials. In Extended Data Fig. 3, we show the results of thermometry performed on dressed clouds but with ramps of varying duration. Although no thermal difference is detected in this case beyond 100-ms ramp time, qualitative inspection of the dressed clouds suggests changes in density distributions as ramp time is varied.

As discussed in ref.<sup>39</sup>, the step size of any non-continuous frequency ramp impacts the adiabaticity of shell inflation; in Extended Data Fig. 4, we show the results of varying the number of discrete frequency steps in a given ramp of (relatively large) amplitude 600 kHz and duration 400 ms, with the initial radiofrequency knife set significantly above  $T_c$  to yield sufficient absorption signal at this shell size. The limit of graining (2,000 points) was set by CAL hardware and operational parameters. A clear increase in temperature (Extended Data Fig. 4, top) was associated with sequences of 500 steps (1,200 Hz per step) with inconclusive behaviour for finer graining. Qualitative inspection of the associated dressed clouds suggested a change in density distribution associated with the 500-step ramps, as shown in Extended Data Fig. 4 (bottom).

As a result of these investigations, the datasets of Fig. 3 are taken with dressing ramps of 300 kHz amplitude and 400 ms duration, with 1,000 frequency steps (0.75 kHz ms<sup>-1</sup> sweep rate, 300 Hz per step).

### Data availability

The datasets generated and analysed in Methods are available from the corresponding author upon reasonable request. All NASA CAL data are on a schedule for public availability through the NASA Physical Science Informatics (PSI) website (<https://www.nasa.gov/PSI>).

### Code availability

Calculation and analysis codes from the Methods are available upon reasonable request from the corresponding author.

56. Pethick, C. J. & Smith, H. *Bose-Einstein Condensation in Dilute Gases* (Cambridge Univ. Press, 2008).
57. Pitaevskii, L. & Stringari, S. *Bose-Einstein Condensation and Superfluidity* (Oxford Univ. Press, 2016).
58. Bagnato, V., Pritchard, D. E. & Kleppner, D. Bose-Einstein condensation in an external potential. *Phys. Rev. A* **35**, 4354–4358 (1987).
59. Houbiers, M., Stoof, H. T. C. & Cornell, E. A. Critical temperature of a trapped Bose gas: mean-field theory and fluctuations. *Phys. Rev. A* **56**, 2041–2045 (1997).
60. Burrows, K. A., Perrin, H. & Garraway, B. M. Nonadiabatic losses from radio-frequency-dressed cold-atom traps: beyond the Landau-Zener model. *Phys. Rev. A* **96**, 023429 (2017).

**Acknowledgements** We thank the NASA/JPL Cold Atom Lab team for their support. Designed, managed and operated by Jet Propulsion Laboratory, the Cold Atom Lab is sponsored by the Biological and Physical Sciences Division of NASA's Science Mission Directorate at the agency's headquarters in Washington and the International Space Station Program at NASA's Johnson Space Center in Houston. We also thank B. Garraway and E. Bentine for input.

**Author contributions** R.A.C. designed experiments, guided data collection and wrote analysis software. D.C.A. conceived the study, designed experiments, guided data collection, operated the CAL instrument, provided scientific guidance and prepared the manuscript. B.R. performed modelling calculations, prepared the manuscript and provided theory support. S.V. and C.L. conceived the study, guided model calculations, and provided scientific guidance and theory support. J.D.M. prepared the manuscript and wrote analysis software. E.R.E. and J.R.W. and R.J.T. operated the CAL instrument and guided data collection; R.J.T. and J.R.W. also provided guidance as CAL project scientists. N.L. conceived the study, designed experiments, guided data collection, performed data analysis and prepared the manuscript. All authors read, edited and approved the final manuscript.

**Competing interests** The authors declare no competing interests.

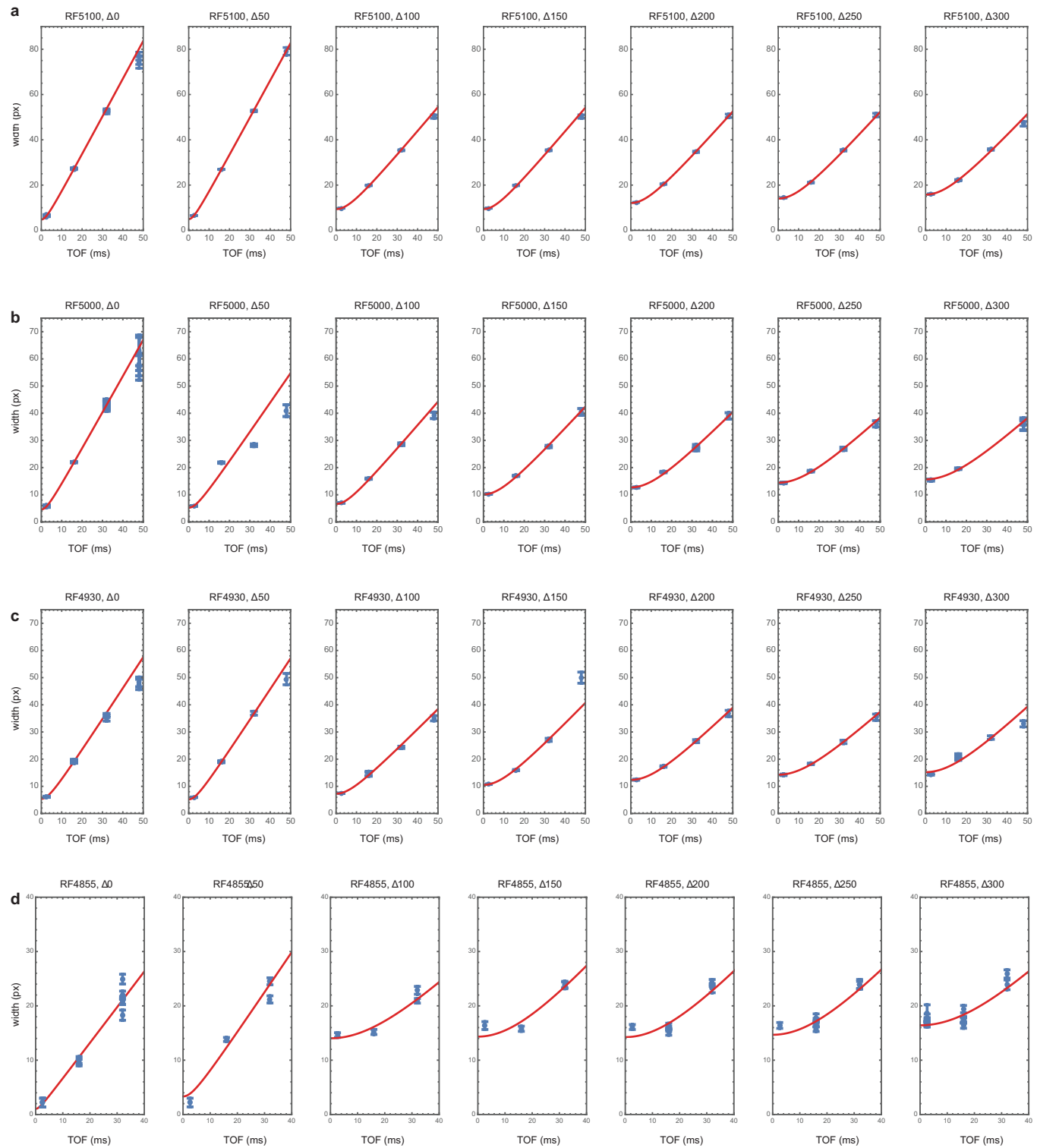
#### Additional information

**Correspondence and requests for materials** should be addressed to N. Lundblad.

**Peer review information** *Nature* thanks Chandra Raman and the other, anonymous, reviewer(s) for their contribution to the peer review of this work.

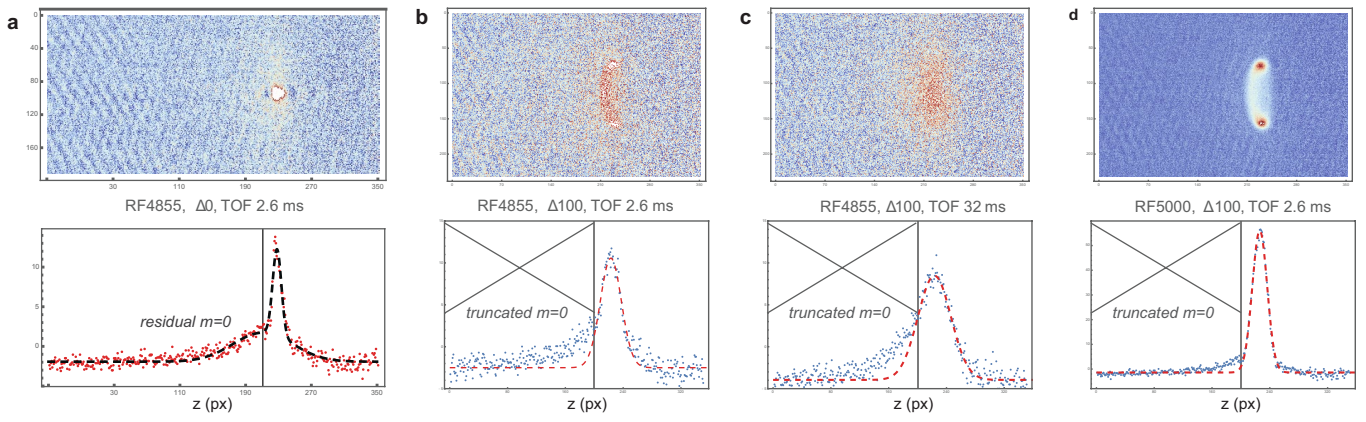
**Reprints and permissions information** is available at <http://www.nature.com/reprints>.

# Article



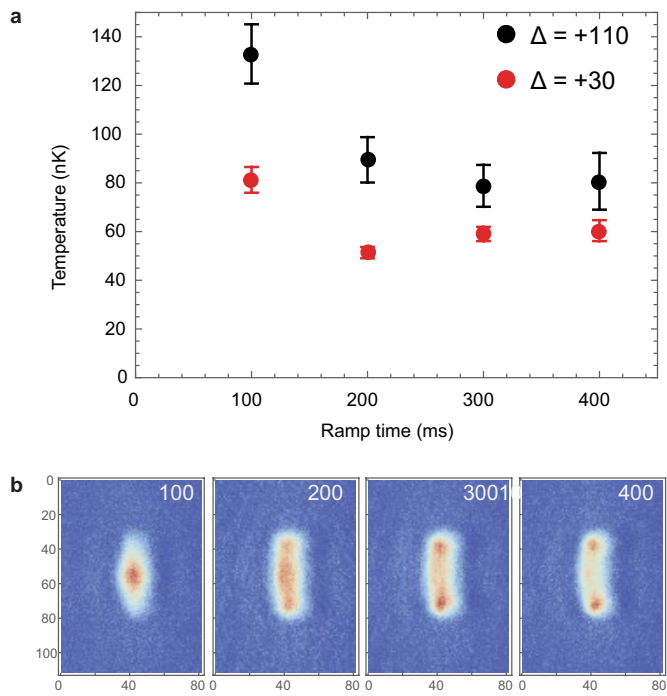
**Extended Data Fig. 1 | Thermometry fitting results.** Cloud size versus time-of-flight fits for initial temperatures as set by rf evaporation, with frequency values given by **a**, 5.1 MHz, **b**, 5.0 MHz, **c**, 4.93 MHz, and **d**, 4.855 MHz,

corresponding to the temperature data in Fig. 3a-d. Error bars represent standard errors.



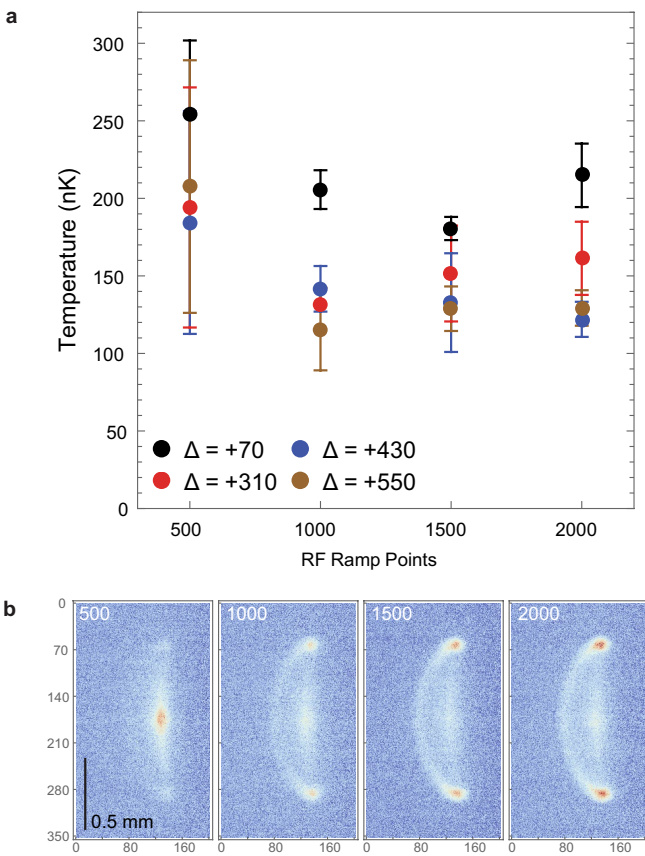
**Extended Data Fig. 2 | Halo rejection.** Details of mechanism for rejecting  $|F=2, m=0\rangle$  halos originating in evaporative cooling, which otherwise would distort thermometry fits of shell structures relevant main text Fig. 3 in the main text. **a**, To proceed we first find (for a typical partially-condensed cloud) the approximate center of the halo marked by a vertical line. This location guides our nearby placement of a truncation region in the fits shown in **b–d** for three

different use cases: **b**, a cold shell of moderate size and short TOF; **c**, a cold shell of moderate size and long TOF; **d**, a warmer, higher atom number shell of moderate size and short TOF. Truncation of a halo-dominant region improves fit capture of relevant shell features, with results shown in dashed red lines. More detail of the halo nature can be found in ref.<sup>21</sup>.



**Extended Data Fig. 3 | Effects of ramp-time variation.** **a**, Ramp time is varied 100–400 ms, with a 1,000-point frequency ramp extending 200 kHz upward from an initial frequency of 2.05 MHz +  $\Delta$ , corresponding to variation in ramp speed 0.5–2.0 kHz/ms. Error bars (where visible) represent standard errors.

**b**, Absorption imaging of  $\Delta = +30$  kHz clouds associated with marked ramp times (associated with red points above). For this dataset initial cloud temperature was set slightly below  $T_c$ , similar to that used in Fig. 3d.



**Extended Data Fig. 4 | Effects of graining variation.** **a**, Graining of the dressing ramp is varied, with resulting dressed-sample thermometry plotted as a function of the number of frequency steps. Error bars (where visible) represent standard errors. All dressing ramps extended 600 kHz upward from an initial frequency of 1.65 MHz +  $\Delta$ , over 400 ms (ramp speed 1.5 kHz/ms), thus varying the step size from 300–1200 Hz. For this dataset initial cloud temperature was set significantly above  $T_c$ , similar to that used in Fig. 3b.

**b**, Dressed ( $\Delta = +550$  kHz, i.e. a ramp 2.2–2.8 MHz) clouds at short (2.6 ms) TOF associated with each rf frequency step graining; note qualitative difference associated with 500-point graining.